Available online at www.sciencedirect.com
ScienceDirect
Carbohydrate Polymers 69 (2007) 467–477
Carbohydrate Polymers
www.elsevier.com/locate/carbpol

N-Acylated chitosan stabilized iron oxide nanoparticles as a novel nano-matrix and ceramic modification

Shanta Raj Bhattarai [a], Remant Bahadur K.C. [a], Santosh Aryal [a], Myung Seob Khil [b], Hak Yong Kim [c,*]

[a] *Department of Bionano System Engineering, Chonbuk National University, Jeonju 561-756, Republic of Korea*
[b] *Center for Healthcare Technology Development, Chonbuk National University, Jeonju 561-756, Republic of Korea*
[c] *Department of Textile Engineering, Chonbuk National University, Jeonju 561-756, Republic of Korea*

Received 29 October 2006; received in revised form 29 December 2006; accepted 8 January 2007
Available online 19 January 2007

Abstract

The present study dealt with the use of hydrophobically modified polycations (*N*-acylated chitosan, *Nac*) stabilized iron oxide nanoparticles (IOPs) as a three dimensional (3D) nano-matrix for the controlled fabrication of hydroxyapatite (HAP). Among three different fatty acid chlorides (hexanoyl, octanoyl, and myristoyl chloride) modified chitosan (*Nac*-6, *Nac*-8, and *Nac*-14, respectively), we demonstrated the *Nac*-6-IOPs as a novel 3D nano-matrix for the controlled fabrication of HAP due to its well dispersibility and stability in aqueous medium (pH 7.4). Thermogravimetric analysis (TGA) estimated that an average two *Nac*-6 molecules could interact with one IOPs when the weight ratio of *Nac*-6 to IOPs was 0.16. Fourier transforms infrared (FT-IR) spectroscopic showed that the interaction of the polymer with IOPs was through the amide group of *Nac*-6. Transmission electron microscopy (TEM) revealed that the *Nac*-6-IOPs were well stable, uniform and mono-disperse in aqueous medium (pH 7.4), with average size of 10 nm. X-ray diffraction (XRD) and FT-IR analysis showed the evidence of HAP formation on the surface of *Nac*-6-IOPs. Scanning electron microscope (SEM) equipped with energy dispersive X-ray (EDX) analysis showed that the HAP on the surface of 3D *Nac*-6-IOPs nanomatrix looks an interesting morphology like quasi-spherical structured with a significant rough surface and highly compact configuration. EDX data analysis confirmed that Ca/P ratio is in excellent agreement with the closer theoretical value of 1.67 for natural HAP. Our investigation for the growth of HAP on the surface of *Nac*-6-IOPs approved that the functional groups and the geometry of the nano-matrix play a key role for inducing and directing the growth of HAP crystals mimicking to that of natural apatite.

Keywords: Biomineralization; Biomaterial; Chitosan; Nanoparticles; Hydroxyapatite

1. Introduction

Functionalization of nanomaterials with chemical or biological molecules exhibits novel properties for various potential applications. The unique physico-chemical properties of these materials when utilized in conjunction with the remarkable biomolecular recognition capabilities could lead to miniature biological, optical and electronics devices. However, an important issue for *in vivo* application is its biocompatibility. Central focus to tackling this issue is surface modification of nanomaterials to prevent the spontaneous aggregation and elucidating the interface between nanomaterials and biosystem. Among inorganic nanomaterials, iron oxide nanoparticles (IOPs) have a high potential for the use in a lot of *in vitro* and *in vivo* applications. Based on their unique mesoscopic physical, chemical, thermal, and mechanical properties, IOPs offer a high potential for several biomedical applications (Berry & Curtis, 2003; Pankhurst, Connolly, Jones, & Dobson, 2003), such as: (a) cellular therapy, cell labelling, and targeting as a tool for cell-biology research (Berry, Wells, Charles, Atchison, & Curtis, 2004); (b) tissue repair (Bulte et al., 2001);

* Corresponding author. Tel.: +82 63 270 2351; fax: +82 63 270 2348.
E-mail address: khy@moak.chonbuk.ac.kr (H.Y. Kim).

0144-8617/$ - see front matter © 2007 Elsevier Ltd. All rights reserved.
doi:10.1016/j.carbpol.2007.01.006

(c) drug delivery (Jain, Morales, Sahoo, Leslie-Pelecky, & Labhasetwar, 2005; Zhang, Kohler, & Zhang, 2002); (d) magnetic resonance imaging (MRI) (Arbab et al., 2005); (e) hyperthermia (Sato, Iijima, Sekin, & Inagaki, 1987); (f) magnetofection (Scherer et al., 2002); etc. For these applications surfaces modification of the nanoparticles by creating a few atomic layer of organic (e.g. polymers) or inorganic (e.g. gold) material or oxide surfaces (e.g. silica or alumina) could be an excellent job for the further functionalization with various bioactive molecules.

Recently, much attention has been given on chitosan as a capping agent due to its out standing biological properties (Khor & Lim, 2003; Robert & James, 1977), such as biocompatibility, biodegradability, antibacterial and wound healing activity. Systematic exploration of chitosan as a structural material has been done for designing functional layers on the electrode surface (Coche-Guerente & Desbrieres, 2005). Moreover, chitosan has been used to make organic–inorganic hybrid materials (Ayer, Elvan, & Nesrin, 2000; Chang & Chen, 2005; Lee, Kim, Shao, & Kwak, 2005; Ramay, Li, Shum, & Zhang, 2005; Silva et al., 2005). However, the application of chitosan and chitosan-based materials is somehow limited by their poor solubility, reactivity, physical properties (e.g. rigidity and britility) and consequently strong intra and inter-molecular hydrogen bonding in aqueous medium. It is expected that the biological and physiological potentialities of chitosan can be improved dramatically, if a water-soluble chitosan or chitosan-based material is prepared. Chemical modifications have been selected to be an excellent job for the preparation of chitosan derivatives with higher solubility in water, such as *O*-, *N*-carboxymethyl-chitosan 15. (Chang & Chen, 2005; Marguerite, Pham, Claude, & Michel, 1992), *N*-carboxymethyl-chitosan (Muzzarelli, Tanfani, Emanuelli, & Mariotti, 1982), *O*-carboxymethyl-chitosan (Lillo & Matsuhiro, 1997; Muzzarelli, 1988), *N*-sulfate-chitosan (Holme & Perlin, 1997), *O*-sulfate chitosan (Focher, Massoli, Torri, Gervasini, & Morazzoni, 1986), *O*-succinyl-chitosan (Zhang, Ping, Zhang, & Shen, 2003), *N*-methylene phosphonic chitosan (Heras, Rodriguez, Ramos, & Aguiio, 2001), hydroxypropyl chitosan (Xie, Xu, Wang, & Liu, 2002), *N*-trimethyl chitosan (Jia, Shen, & Xu, 2001), etc.

Focusing on general way to improve the solubility of chitosan, present study dealt with the chemical modification of the chitosan with different fatty acid chlorides. It has been reported that after acylation with fatty acid chlorides, the possible inter- and intra-molecular hydrogen bodings of chitosan are replaced by hydrophobic interaction which are believed to enhance its solubility (Tien, Lacroix, Ispas-Szabo, & Mateescu, 2003). Nevertheless, the solubility depends on the chain length of acyl chloride. Recently, among different acyl chloride, hexanoyl chloride modified chitosan (hexanoyl chitosan) has been widely applicable in engineering fields (Choi, Kim, Pak, Yoo, & Chung, 2007; Neamnark, Rujiravanit, & Supaphol, 2006; Peesan, Supaphol, & Rujiravanit, 2005; Tien et al., 2003).

On the other hand, calcium phosphates are attractive biomedical materials owing to their excellent biocompatibility and non-toxicity. There are many phases of calcium phosphates. Among them, hydroxyapatite (HAP) is the most ubiquitous and well-known phase studied for a number of biomedical applications owing to its similarity to natural bone. Basically, to grow HAP either biologically or biomimetically two-dimensional (2D) templates have been used (Ayer et al., 2000; Ramay et al., 2005; Silva et al., 2005). However, these templates could not provide a significant control over size and morphology of HAP crystals. To overcome this limitation, different types of three-dimensional (3D) templates viz: polymeric and biocompatible hydro gel scaffolds, polyelectrolyte capsules, aluminum oxide, etc. have been frequently used (Shchukin, Sukhorukov, & Mohwald, 2003; Song, Malathong, & Bertozzi, 2005). Rautaray et al. first time used the amino acid capped gold nanoparticles as a 3D template for the growth of HAP crystals (Rautaray, Mandal, & Sastry, 2005). Later Kc et al. used the modified chitosan stabilized gold nanoparticles as a 3D template for the controlled fabrication of HAP crystals (Kc, Aryal, Bhattarai, & Kim, 2006). However, to the best of our knowledge, there has been no previous report about the use of functionalized iron oxide nanoparticles (magnetic particles) as a 3D template for the growth of HAP crystals, although S.H. Cartmell for the first time has demonstrated the development of magnetic particles for long-term culture of bone cells with intermittent mechanical activation (Cartmell, Dobson, Verschueren, & EI Haj, 2002). Focusing on above research, we also purposed the application of functionalized iron oxide nanoparticles (magnetic particles) for the control fabrication of HAP so as to make a better candidate in bone tissue engineering.

In this paper, chemical modification of natural chitosan was done through *N*-acylation *(Nac)* using three different fatty acid chlorides (hexanoyl, octanoyl, and myristoyl chloride) and subsequently used them for the stabilization of IOPs. Among the nanoparticles, we have selected the hexanoyl chloride modified chitosan stabilized iron oxide nanoparticles (*Nac*-6-IOPs) as a novel 3D nano-matrix for the controlled fabrication of HAP due to its well dispersibility and stability in aqueous medium (pH 7.4).

2. Experimental section

2.1. Materials

Iron (III) chloride hexahydrate ($FeCl_36H_2O$) pure granulated, 99%, iron (II) chloride tetrahydrate ($FeCl_24H_2O$) 99+%, and ammonium hydroxide (14.8 M) were purchased from Fisher Scientific (Pittsburgh, PA). Deionized water purged with nitrogen was used in all the steps involved in the synthesis and formulation of iron oxide nanoparticles. Chitosan-100 [viscosity average molecular weight, $M_v = 1.3 \times 10^5$, degree of deacetylation (fraction of free

amino group) 78%] was purchased from Wako Pure Chemical Industries, Ltd., Japan.

2.2. Synthesis of iron oxide nanoparticles (IOPs)

Aqueous solutions of 0.1 M Fe(III) (30 ml) and 0.1 M Fe(II) (15 ml) were mixed, and 3 ml of 5 M ammonia solution was added dropwise over 1 min with stirring on a magnetic stir plate. The stirring continued for 20 min under a nitrogen-gas atmosphere. The particles obtained were washed 3 times using ultracentrifugation (25,000*g* for 20 min at 4 °C) with nitrogen-purged water. The IOPs yield was determined by weighing of the lyophilized sample of the preparation, was 304 mg.

2.3. Preparation of N-acylated chitosan (Nac)

Preparation of *N*-acylated chitosan (*Nac*) was taken form previously described report (Kc et al., 2006). Briefly, a mixture of chitosan-100 (0.83 g) and 1.0% aqueous acetic acid (100 ml) was stirred for 24 h to ensure complete solubility. The pH was adjusted to 6.3 by slow addition of 0.1 M of NaOH with strong agitation, yielding gel slurry. After addition of 0.02 M of fatty acyl chloride (hexanoyl chloride, FW = 134.61, $d = 0.978$ g/ml), the resultant solution was diluted 11 times with de-ionized water. Similar procedure was taken for other acyl chloride (octanoyl, FW = 162.66, $d = 0.949$ g/ml; and myristoyl, FW = 246.82, $d = 0.913$ g/ml; chloride). After 6 h of continuous stirring, the solution was neutralized (pH 6.8–7.5) by 0.1 M of NaOH and precipitated with acetone. The precipitate was collected by filtration and washed with excess of methanol (50–60 °C). The washing was repeated 4 times, and finally the products were dried under vacuum for 3 days at room temperature.

2.4. Stabilization of iron oxide nanoparticles (Nac-IOPs)

Polymer (*Nac*, 5.0 ml of 0.33% in N/10 HCl) was added to the dispersion of the nanoparticles (100 mg) (the dispersion was cooled to room temperature but not lyophilized) and reacted overnight under nitrogen. These particles were washed with nitrogen-purged water to remove soluble salts and excess polymer. Particles were separated by ultracentrifugation at 25,000*g* (Optima LE-80 K, Beckman, Palo Alta, CA) using a fixed angle rotor (50.2 Ti) for 30 min at 10 °C. The supernatant was discarded, and the sediment was redispersed in 15 ml of triply distilled water by sonication (FS-30, Fisher Scientific) for 10 min. The suspension was centrifuged as above, and the sediment was washed three times with triply distilled water. Nanoparticles were resuspended in triply distilled water by sonication as above for 20 min and centrifuged at 12,000*g* for 20 min at 7–11 °C to remove any large aggregates. Here, we have prepared three different types of modified chitosan stabilized IOPs (*Nac*-6-IOPs, *Nac*-8-IOPs, and *Nac*-14-IOPs). Among the nanoparticles, *Nac*-6-IOPs was selected as a material of interest due to its well dispersibility and stability in aqueous medium (pH 7.4) (Fig. 1).

2.5. Ceramic modification of Nac-IOPs (Nac-6-IOPs-HAP)

Ceramic modification of *Nac*-6-IOPs was done by *in situ* nanoprecipitation technique as reported earlier (Aryal, Kc, Dharmaraj, Kim, & Kim, 2006). Representative process is shown in Scheme 1. Briefly, aqueous *Nac*-6-IOPs solution (10 mg, 50 ml) was aged with calcium chloride solution (0.02 M, 5 ml) for 1 h. To this mixture disodium hydrogen phosphate (0.01 M, 5 ml) was dropped under constant stirring at 37 °C, and pH was maintained at 7.4 with the addition of HCl or NaOH solution. After some time, color of the reaction mixture was changed to muddy white that indicates the deposition of HAP on *Nac*-6-IOPs. After calculated time (1, 2, and 3 h), the resultant product was collected using centrifuge at 12,000*g* for 10 min at 4 °C, and washed with triply distilled water. Further analysis, was performed by dispersing the product in deionized triply distilled water at pH 7.4.

2.6. Characterization

Fourier-transform infrared (FT-IR) spectra were recorded as KBr pellets using ABB Bomen MB 100 spectrometer. X-ray diffraction (XRD) analysis on glass substrates was carried on Rigaku, *D*/max 2500 defractrometer with Cu, Kα ($\lambda = 0.154$) source. Thermogravimetric analysis (TGA) was carried in 2010 thermo

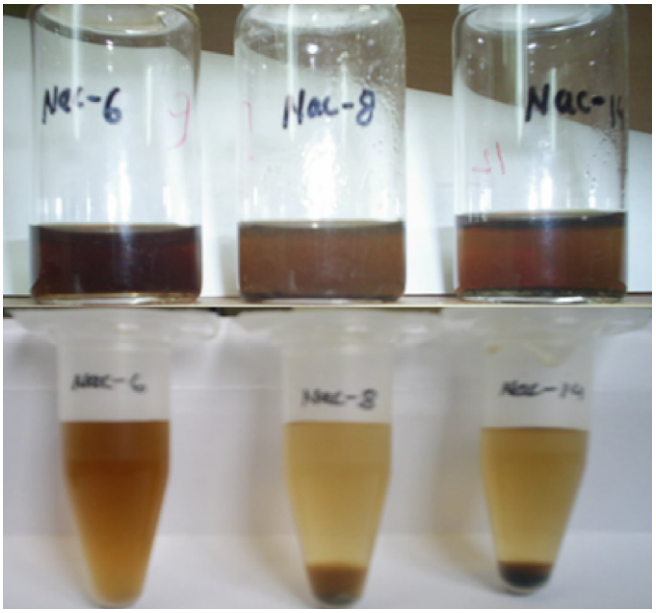

Fig. 1. Stability of different *N*-acylated chitosan (*Nac*-6, *Nac*-8, and *Nac*-14, from left to right, respectively) modified IOPs at physiological pH 7.4. Upper and lower panel represents the freshly prepared and after storage for 1 month at 4 °C, respectively. Lower panel (*Nac*-8 and *Nac*-14) demonstrates that the sedimentation occurs at the bottom of tube with black color.

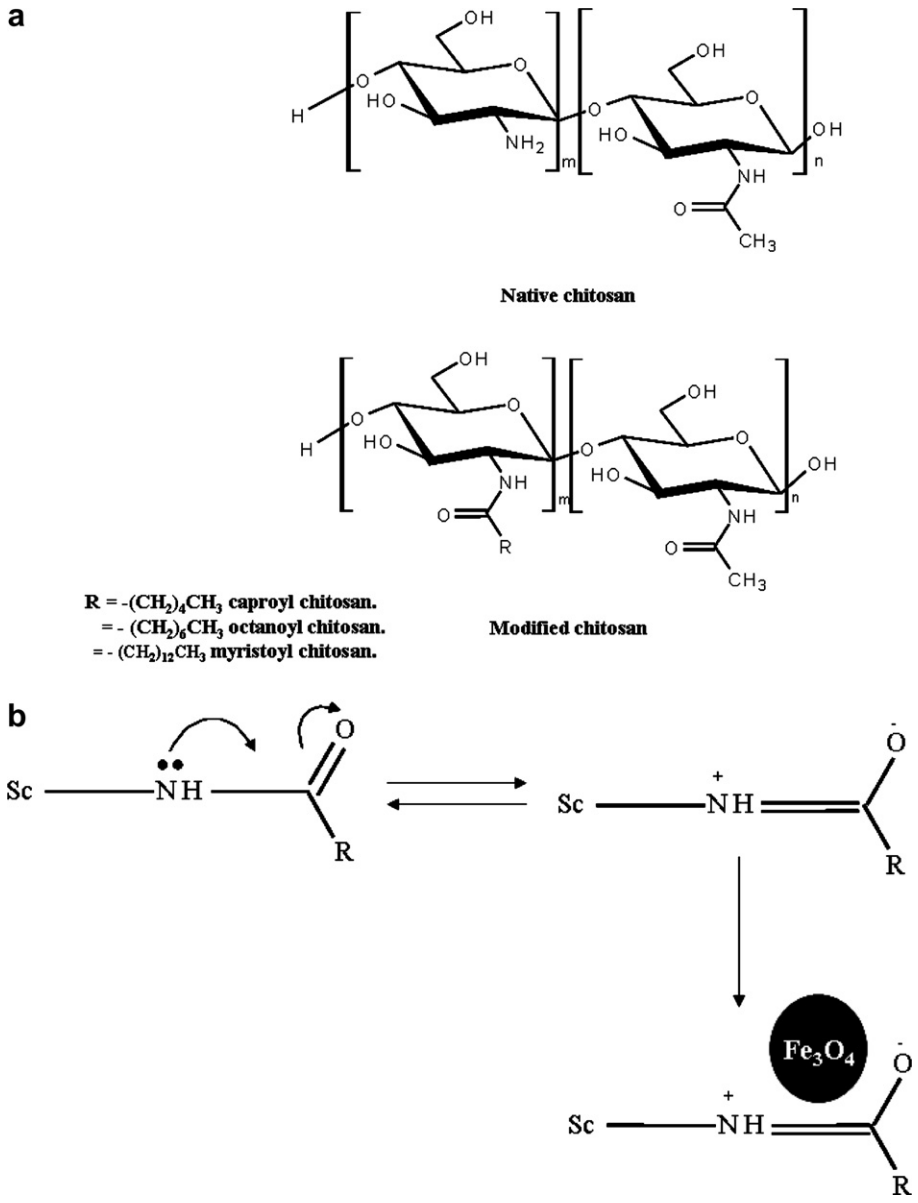

Scheme 1. Schematic representation, (a) chitosan derivatization with fatty acyl chlorides, and (b) possible interaction between IOPs and *Nac*-6. The subscripts *m* and *n* represent the variable units. Sc and R represent the saccharine ring and alkyl groups, respectively.

gravimetric analyzer at a heating rate of 15 °C min^{-1} from room temperature to 1000 °C, under a steady flow of nitrogen. The amounts of *Nac*-6 bound on the magnetic nanoparticles were estimated by the percentage weight losses from the corresponding TGA curves. Morphology and elemental analysis was observed on JEOL GSM scanning electron microscope (SEM) equipped with energy dispersive X-ray (EDX) analysis. Particle size and morphology were observed by JEOL JEM 2010 transmission electron microscope (TEM) operating at 200 kV. Samples for TEM were prepared by dipping a carbon-coated copper grid in an aqueous dispersion of the sample powder and dried at room temperature. Before each analysis, samples were sonicated in an ultra-sonicator bath for 1 min.

3. Results and discussion

3.1. Chemical modifications of chitosan (Nac)

The chemical modification of native chitosan (Scheme 1a) and its complete description were taken from previous publication (Kc et al., 2006). Briefly, the spectrum of native chitosan exhibited the characteristic bands at 1656 cm^{-1} (amide I), 1593 cm^{-1} (amide II), and 1373 cm^{-1} (amide III) (Fig. 2a, curve A) (Chang & Chen, 2005; Marguerite et al., 1992). After acylation, the intensity of amide I was significantly increased as compared to amide II, which shows the partial acylation of chitosan (Fig. 2a, curve B). If it were fully acylated, the amide II band would have completely disappeared (Choi et al., 2007; Neamnark

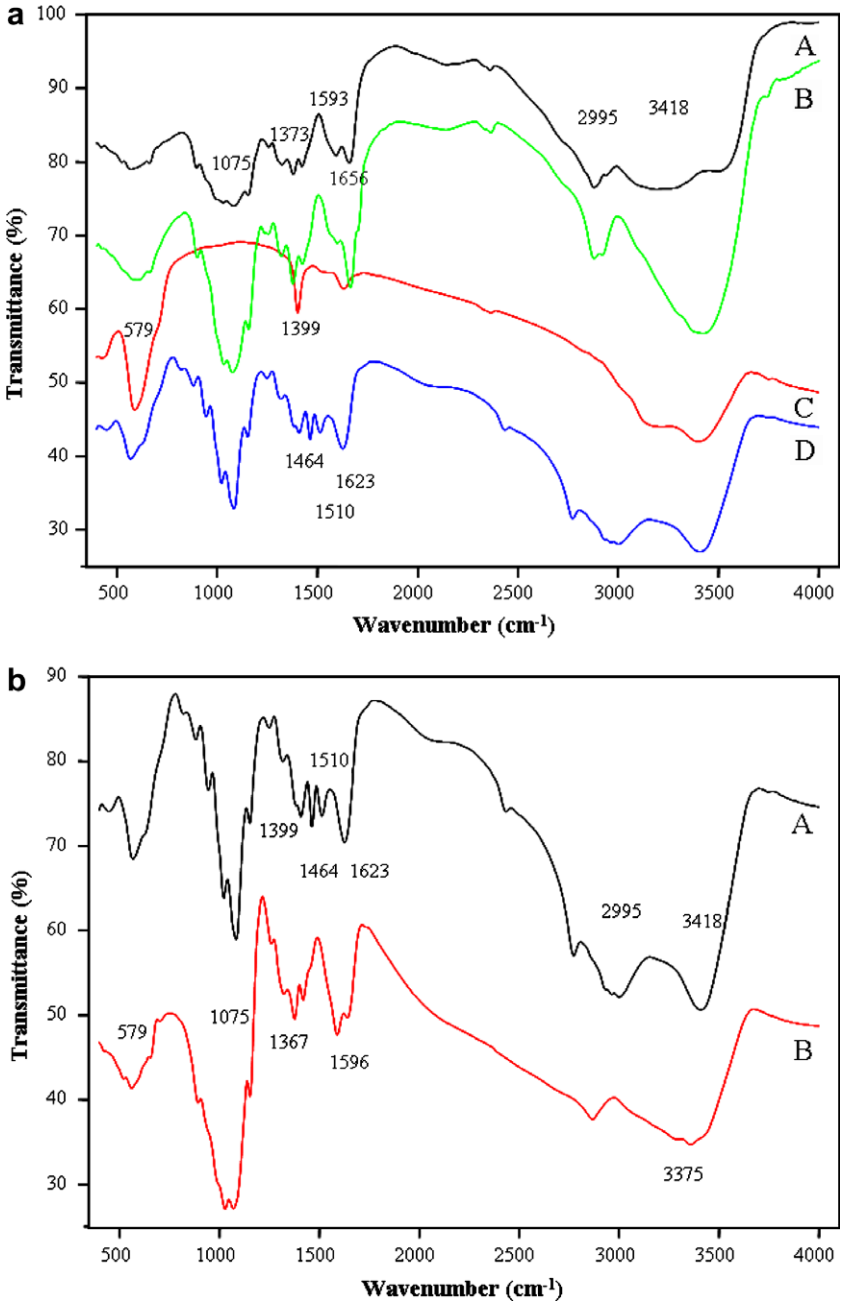

Fig. 2. FT-IR spectra of: (a) native chitosan (A), modified chitosan (*Nac*-6) (B), iron oxide nanoparticles (IOPs) (C) and *Nac*-6-IOPs (D); (b) *Nac*-6-IOPs (A) and Nac-6-IOPs-HAP (B).

et al., 2006; Peesan et al., 2005; Tien et al., 2003). Furthermore, the appearance of a shoulder peak at 2895 cm^{-1} due to C—H stretching confirms the alkyl substitution in chitosan backbone. Intensity of this band linearly increased with the chain length of acid chloride. A broad band in the region of 3200–3500 cm^{-1} in all the cases was assigned to the H-bonded N—H and O—H stretching vibrations (Bhattarai, Edmondson, Veiseh, Matsen, & Zhang, 2005). The spectra of all the compounds showed a well-resolved band due to C—O stretching of saccharine moiety at 1075 cm^{-1} (Daniel & Astruc, 2004; Wyrna & Beyer, 2002). Though, the acylation was performed under identical condition, the degree of acylation was different with the types of fatty acyl chlorides, i.e.; 45.2% for the *Nac*-6.

3.2. Stabilization of iron oxide nanoparticles (Nac-IOPs)

Fig. 1 demonstrates the stability of different *N*-acylated chitosan (*Nac*-6, *Nac*-8, and *Nac*-14) stabilized IOPs at physiological pH 7.4. After 1 month of storage at 4 °C, *Nac*-8 and *Nac*-14 stabilized IOPs showed some aggregation and settle down, where as *Nac*-6 stabilized IOPs did not show that aggregation. This is our clear evidence that *Nac*-6 stabilized IOPs has better stability up to 1 month

under 4 °C and subsequently we have characterized *Nac*-6 stabilized IOPs in details. Fig. 2a shows the FT-IR spectra of IOPs and *Nac*-6-IOPs (curves C and D). The spectra of IOP exhibit strong bands in the low frequency region below 800 cm^{-1} due to the IOPs skeleton. In other regions, the spectra of IOPs have weak bands. The spectrum is consistent with magnetic Fe_3O_4 and the signals associated to the magnetite appear as broad features at 408.9, 571.5, and 584.5 cm^{-1} (Gupta, Berry, Gupta, & Curtis, 2003).

Similarly, the characteristic bands of modified chitosan, amide I, II, and III were shifted to 1623, 1510, and 1464 cm^{-1} on the interaction with IOPs. Shifting of such amide bands either higher or lower energies indicates the attachment of IOPs with modified chitosan through the amide bond region. The potential sites for the interaction of IOPs with chitosan are its free amine group and the carbonyl oxygen (N—C═O). Indeed, nitrogen atoms of amine group hold a free electron doublet that is responsible for the uptake of metal ions by a chelation mechanism (Ayer et al., 2000; Chang & Chen, 2005; Lee et al., 2005; Silva et al., 2005). In addition, we thought that the resonance effect of π-electrons (carbonyl bond) and doublets electron (nitrogen) leads to increase a reasonable electronic density, which facilitate the possible electrostatic interaction between IOPs and chitosan (Scheme 1b) (Jain et al., 2005). Such interaction was spectroscopically conformed by the significant blue shift in the amide bands (Fig. 2a). Likewise, the broad band (H-bonded N—H and O—H) at 3200–3500 cm^{-1} modified to an intense peak, which is probably due to decrease in the extent of H-bonding and interaction with metallic surface (Brewer & Selina, 2002).

The TGA and DTA curves of naked and *Nac*-6-IOPs are shown in Fig. 3. For naked IOPs, TGA curve shows a weight loss at 100–200 °C. The weight loss over this temperature was about 3%. This might be due to the loss of residual water in the sample. No significant peak appeared in the DTA curve beyond 200 °C, Fig. 3B. Similarly, the TGA curve of the *Nac*-6 showed two weight loss steps. The 1st step observed at 100 °C characterized to be due to the residual water where as the 2nd step observed at 318 °C attributed to be due to burning of the polymers (Kc et al., 2006). On the other hand, for *Nac*-6-IOPs, the TGA curve shows two weight loss steps. The first weight loss step around the temperature 100 °C might be due to the loss of residual water in the sample. The sharp weight loss at 238 °C was due to the burning of *Nac*-6. There was no significant peak appeared in the DTA curve beyond 400 °C, implying the presence of only iron oxide within the temperature range. From the percentage weight loss in the TGA curve, the amount of *Nac*-6 bound on the magnetic IOPs was estimated. The experiment was performed in 5 ml of *Nac*-6 solution containing a constant IOPs amount of 100 mg. In our separate experiment, we found, with increasing amounts of *Nac*-6 in solution, the amount of *Nac*-6 bound on the magnetic nanoparticles increased first and then remained

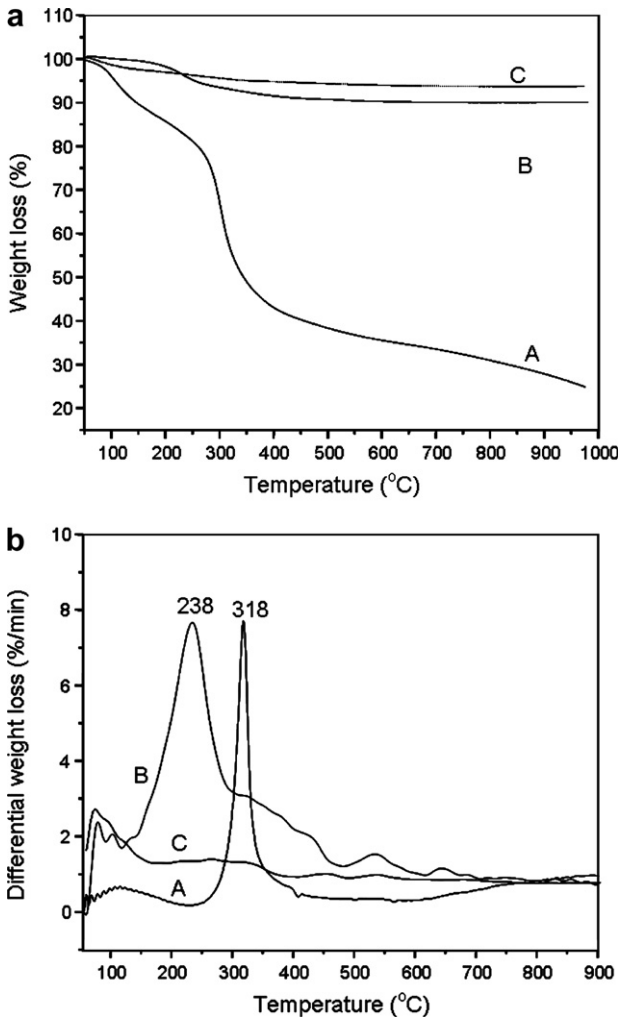

Fig. 3. Thermogravimetric curve (a) and differential thermal analysis (b) of *Nac*-6 (A), *Nac*-6-IOPs (B), and IOPs (C), obtained by heating the samples from room temperature to 1000 °C under a steady flow of nitrogen.

constant at 9 mg when the amount of *Nac*-6 in solution was above 20 mg. Thus, the maximum weight ratio of *Nac*-6 bound to IOPs could be determined to be 0.16. In addition, the density of Fe_3O_4 (IOPs) is 5.18 g cm^{-3} (Liao & Chen, 2002; Woo et al., 2004) and the average molecular weight (viscosity average molecular weight calculated using Brookfield viscometer, 1% solution in 1% acetic acid) of *Nac*-6 was about 1.5×10^6. Assuming the resultant IOPs were spherical, it could be estimated that on average two *Nac*-6 molecules were bound with one IOPs when the weight ratio of *Nac*-6 to IOPs was 0.16.

3.3. Ceramic modification of Nac-IOPs (Nac-6-IOPs-HAP)

The characteristic amide bands of *Nac*-6-IOPs (I, II, and III) at 1623, 1510 and 1464 cm^{-1} were significantly modified to intense and broad band (centered at 1596 cm^{-1} for I and II, 1367 cm^{-1} for III) after the ceramic (HAP) modification (Fig. 2b, curves A and B).

Similarly, the band (H-bonded N—H and O—H) at 3418 cm^{-1} was modified and shifted into an intense band at 3375 cm^{-1}. Further, the C—O stretching vibration at 1075 cm^{-1} corresponding to the saccharine moiety was well intense into a broad band (850–1159 cm^{-1}). The reason behind increased intensity with significant peak broadening was due to the coupling effect of v_1 and v_3 stretching modes of PO_4^{3-} at 960 cm^{-1}, and 1115 and 1010 cm^{-1}, respectively (Aryal et al., 2006). The band corresponds to IOPs at 566 cm^{-1} was well resolved after ceramic modification due to the addition of v_4 mode of PO_4^{3-} groups (Aryal et al., 2006). It implies that the ceramic modification of *Nac*-6-IOPs was initiated through oxygen atom of polymer via ionic interaction as shown in Scheme 2b. Obviously, after addition of Ca^{2+} during ceramic modification were first adsorbed onto the remained active functional groups (—OH, C—O—) of chitosan and than nucleation started under subsequent addition of PO_4^{3-}. Thus, we speculate that the electrostatic interaction between Ca^{2+} with oxygen was the fundamental nucleation steps during the ceramic modification Scheme 2.

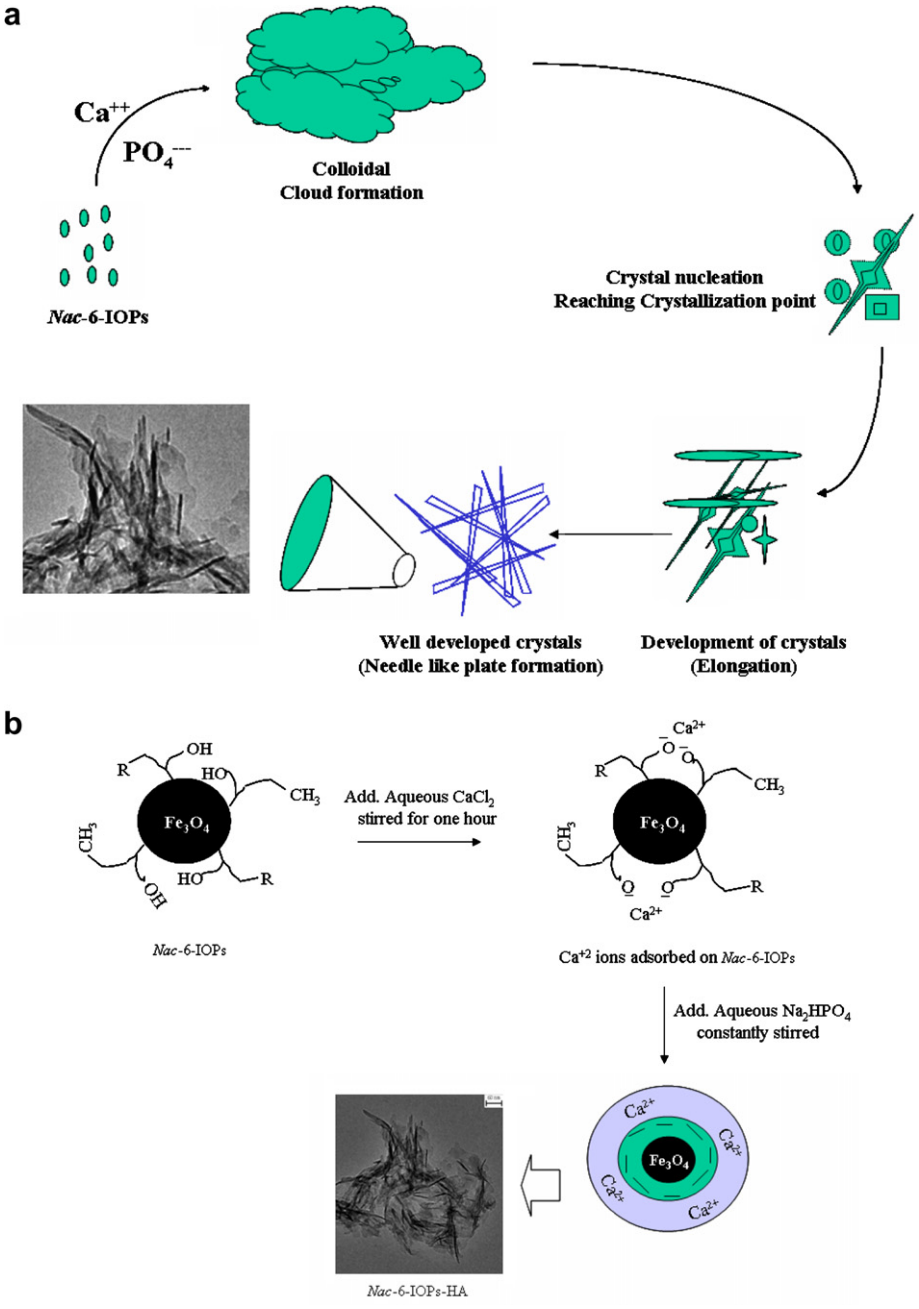

Scheme 2. Schematic representation for the growth of hydroxyapatite (HAP) on *N*-acylated chitosan stabilized iron oxide nanoparticles (*Nac*-6-IOPs). (a) Schematic illustration of the general procedure to produce nanostructure HAP and their resulting morphologies. (b) Illustrate the role of chitosan together with the surface charge and surface functional groups of the resulting modified iron oxide particles on the crystal growth. TEM images represent corresponding to the morphological diagram.

X-ray diffraction pattern of the IOPs, *Nac*-6-IOPs, and *Nac*-6-IOPs-HAP is presented in Fig. 4. It has been reported that IOPs have multivalent oxidation states, abundant polymorphism and the mutual polymorphous changes in nanophases (magnetite; Fe_3O_4, maghemite; γ-Fe_3O_4, hematite; α-Fe_3O_4 and wustite; Fe_3O_4). The XRD pattern of our formulated IOPs matched with magnetite(Fe_3O_4) phase as compared to the standard XRD patterns as reported elsewhere (Liao & Chen, 2002; Woo et al., 2004).The sharp peaks which appeared approximately at 30, 35, 43, 53, 57, and 62° 2θ value were due to Fe_3O_4 (Cheng et al., 2005). Similarly, a broad peak which appeared approximately 20^0 was assigned to the modifying agents (*Nac*-6), (Fig. 4, curve B). Bragg reflections (111), (002), and (112) of HAP attributed to the peaks at 23, 26, and 32° 2θ values of *Nac*-6-IOPs-HAP (curve C) and the broad peak corresponding to *Nac*-6 (curve B) were completely merged to the peak *of Nac*-6-IOPs-HAp. Well resolved Bragg reflections (220), (311), (400), (422), (511), and (440) of IOPs attributed to the peaks at 30, 35, 43, 53, 57, and 62° 2θ value were distinctly observed in the XRD pattern of *Nac*-6-IOPs and *Nac*-6-IOPs-HAP in every case, which indicates the persistence of IOPs in all the samples.

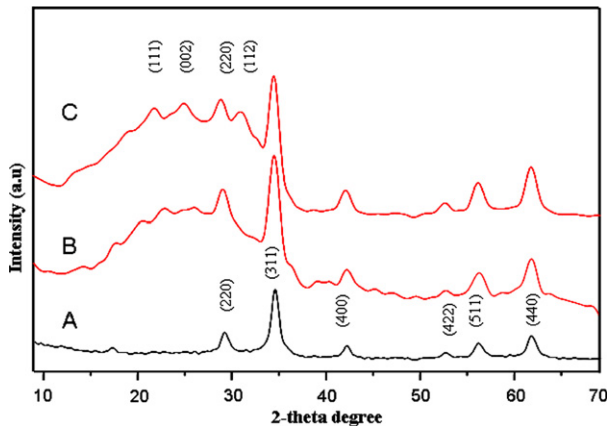

Fig. 4. XRD patterns of: *Nac*-6-IOPs (A), and *Nac*-6-IOPs-HAP (B).

Surface morphology and elemental composition of HAP nanocrystal fabricated on the surface of *Nac*-6-IOPs, were studied by SEM equipped with an EDX analyzer. The representative SEM images of *Nac*-6-IOPs, HAP growth without *Nac*-6-IOPs nanomatrix and Nac-6-IOPs-HAP are presented in Fig. 5. Typical SEM images of *Nac*-6-IOPs (Fig. 5A) show well-dispersed, roughly spherical particles. HAP crystals synthesized by reacting Na_2HPO_4 with Ca^{2+} ions in the absence of *Nac*-6-IOPs nanomatrix were found to be nanocrystals and growth in 2D directions with small rod shape (Fig. 5B). However, same HAP on the surface of 3D *Nac*-6-IOPs nanomatrix showed an interesting morphology like quasi-spherical structured particles of sizes ranging from 1 to 5 μm with a significant rough surface (Fig. 5C and D). The surface of particles was seen more clearly at higher nucleation time that composed of thin platelets in a highly compact configuration (Fig. 5D). The quantitative analysis of HAP nanocrystals fabricated on *Nac*-6-IOPs was done from the intensity of Ca and P signals in the EDX spectra (Fig. 6). It was 1.57 in *Nac*-6-IOPs nearly in agreement with the expected stoichiometry based on the chemical structure of HAP [Ca_{10} $(PO_4)_6(OH)_2$]. However, Ca/P ratio, which we found in this research, was varied with the nucleation time (results not shown).

Fig. 7 shows the TEM images of IOPs, *Nac*-6-IOPs and *Nac*-6-IOPs-HAP. The morphology of IOPs (Fig. 7A) was

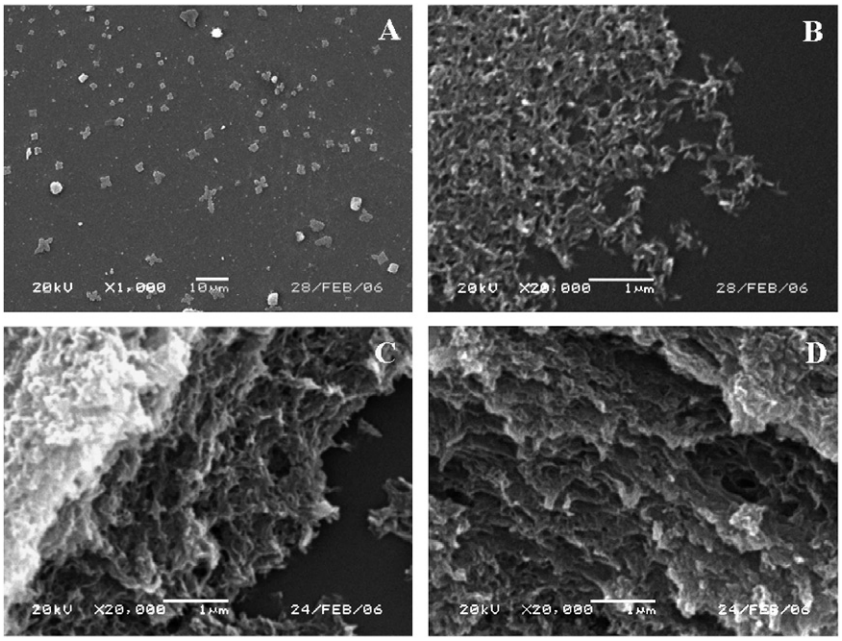

Fig. 5. SEM images recorded from drop-coated films on glass substrates of: *Nac*-6- IOPs (A), HAP control (B), *Nac*-6- IOPs-HA (C) and (D) at different magnification.

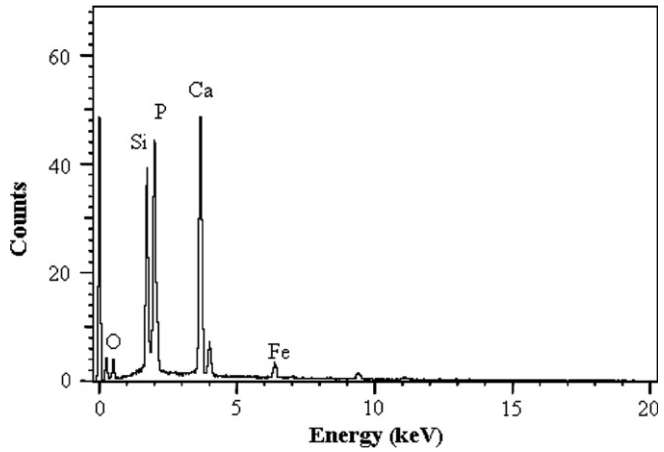

Fig. 6. EDX profile of HAP grown on *Nac*-6-IOPs nano-matrix.

clustered type, which is same morphology as reported elsewhere (Kim, Mikhaylova, Zhang, & Muhammed, 2003). After modification, it was significantly dispersed with an average diameter 10 nm (average over 100 particles) (Fig. 7B) in aqueous medium at pH 7.4. The TEM micrographs further supports the mineralization process as a platelet as described previously (Aryal et al., 2006). The individual platelets were well resolved in the form of needle shaped nanocrystals. Geometry of the particles in *Nac*-6-IOPs was like a simple aggregates where as it was like needles in HAP (Fig. 7C). It implies that the HAP nanocrystals grown on the *Nac*-6-IOPs were needles, where *Nac*-6-IOPs acted as a nucleation centers. TEM images (Fig. 7D) strongly supports SEM (Fig. 5D) that the HAP crystals completely cover the underlying *Nac*-6-IOPs and grow outward from this core with time. The mechanism for the growth of HAP crystals on the surface of *Nac*-6-IOPs can be better explained in Scheme 2. Briefly, matrix mediated bio-mineralization has been divided into two stages: nucleation and growth (Beppu & Santana, 2002a, 2001b). For nucleation, an organic surface may play roles in promoting mineral deposition, physisorption of ions and small precipitates, orientation of crystal lattices, preferential deposition, and heterogeneous nucleation. From our results, we believe that at the physiological condition (pH 7.4), there is significant influence of matrix in the deposition. It is interesting to note that needle-like apatite is one of the main components of natural bone and teeth, while plate like for shells. Still no authors have obtained needle like apatite in chitosan or chitosan based materials, moreover in physiological pH 7.4. We are unable to explain its real mechanism about why our formulated material perfectly gave needle like apatite in physiological pH 7.4. However, we believe, texture of matrix (here, *Nac*-6-IOPs nanomatrix), functional groups of organic matrix (here, —OH, C—O—, and N—C=O functional groups of *N*-acylated chitosan) and also saturated environment of growth

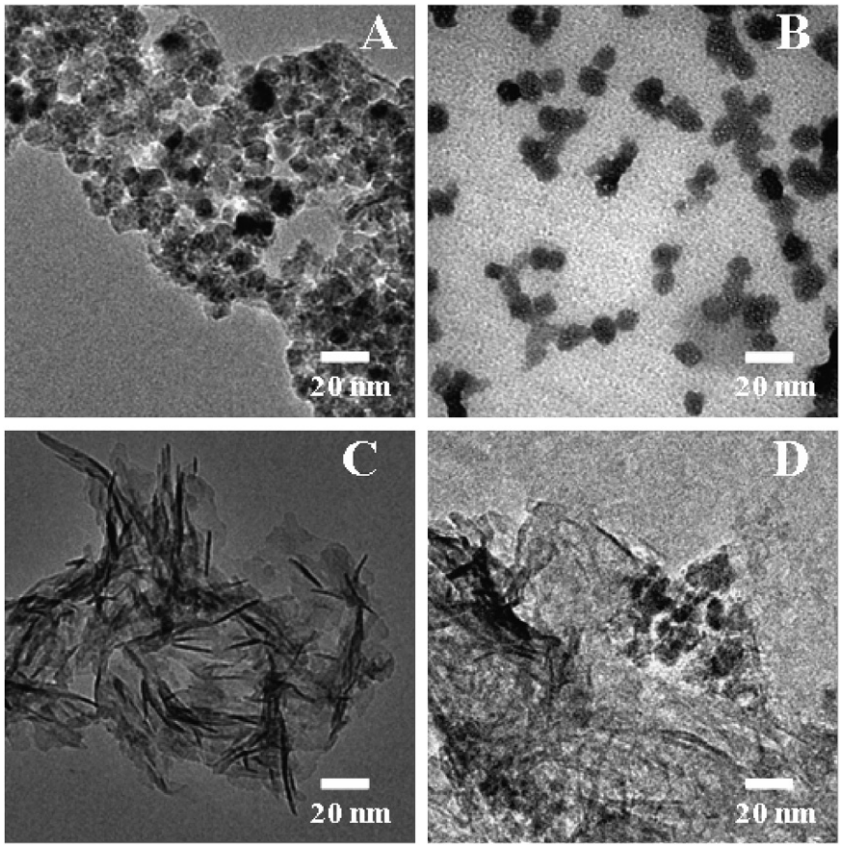

Fig. 7. TEM micrographs of IOPs (A), *Nac*-6-IOPs (B), *Nac*-6-IOPs-HAP (C) and (D) dispersed in triple distilled water at pH 7.4.

fluid could play key roles (here, Ca: $P < 1.5$). For instant, if we consider heterogeneous nucleation, it is believed that, because the chemical bonding at the surface of mineral nuclei is primarily ionic, the organic interface must contain area with high local energy, where electrostatic, dipolar, or hydrogen bonding interactions can take place during nucleation. For example, in the case of silica, it has functional groups (—Si—OH), some of which are dissociated into negatively charged units (—Si—O^-) at around pH 7.0. These negatively group played important roles as nucleating group (Li, Nakanishi, Kokubo, & de Groot, 1993). According to these studies, when nucleation is controlled, needle like apatite forms, organized in clusters, producing results that are very similar to chitosan substrate results regarding morphology and composition. In our present study at physiological condition, chitosan has marjority of its —OH, C—O—, and least amino and carbonyl oxygen (N—C=O) functional groups. All of them considered as the very active site for nucleation steps during ceramic modification.

Diffusion effect, heterogeneous nucleation interconnectivity, critical nucleation size and interface kinetics are the main factors for the crystal growth mechanism. For instant, if we considered the diffusion effect it dependent on Ca:P ratio. Kokubo et al. (1990) reported that the control of apatite formation on silica is directly related to Ca:P ratio on the fluid. The author further discuss that this is probably due to the fact that the Ca:P ratio varies especially close to the frontier of apatite and fluid. At an interface where there is lower quantity of available Ca (Ca: $P < 1.5$), the author found a more granulated morphology. However that morphology is not in agreement with those found in the present study. Finally, Beppu et al. clearly described (Beppu & Santana, 2002a, 2001b), based on two theories about matrix mediated mineralization: (1) deposition depends on the chemical nature of the matrix (Kokubo et al., 1990) and (2) calcification (osteocondition) depends on micromechanics on the surface rather than the chemistry. We believe that both chemical nature and texture of the matrix (here, nanomatrix), could play important role in matrixmediated apatite growth for the variable morphology and form. However, furthermore study is required to elucidate the possible mechanism for the growth of needle shaped apatite, which are undergoing.

4. Conclusions

Aliphatic hydrophobic chain of different length was grafted on to the backbone of chitosan by *N*-acylation using different fatty acid chlorides. Hydrophobic modified chitosan stabilized iron oxide nanoparticles (*Nac*-IOPs) were prepared by graft-onto approach. FT-IR spectroscopic analysis of *Nac*-IOPs confirmed the attachment of polymer on the surface of IOPs was through the amide bonds. TEM observation revealed that the *Nac*-6-IOPs were well dispersed in aqueous medium at physiological pH with uniform size around 10 nm. Hence, we believe that the formulated *Nac*-6-IOPs in aqueous medium at physiological pH could be suitable biomaterials for different applications. The investigation for the control fabrication of HAP using *Nac*-6-IOPs as a novel 3D nano-matrix via *in situ* nano-precipitation technique showed that the nucleation was initiated through the oxygen atom of polymer and dependent on the nucleation time. Further the X-ray diffraction study of these nano-composites showed the existence of IOPs in a magnetite (Fe_3O_4) phase. These organic–inorganic composite materials are expected to play an important role in biomedical application especially in bone tissue engineering.

Acknowledgements

This work was supported by the Korea Research Foundation Grant funded by the Korean Government (MOEHRD) (the Center for Healthcare Technology Development, Chonbuk National University, Jeonju 561-756, Republic of Korea).

References

Arbab, A. S., Wilson, B. L., Ashari, P., Jordan, E. K., Lewis, B. K., & Frank, J. A. (2005). A model of lysosomal metabolism of dextran coated superparamagnetic iron oxide (SPIO) nanoparticles: implications for cellular magnetic resonance imaging. *NMR in Biomedicine, 18*, 383–389.

Aryal, S., Kc, K. B., Dharmaraj, N., Kim, K. W., & Kim, H. Y. (2006). Synthesis and characterization of hydroxyapatite using carbon nanotubes as a nano-matrix. *Scripta Materiala, 54*, 131–135.

Ayer, B., Elvan, Y., & Nesrin, H. (2000). Evaluation of chitosan as a potential medical iron (III) ion adsorbent. *Turkey Journal of Medical Science, 30*, 341–348.

Berry, C. C., & Curtis, A. S. G. (2003). Functionalisation of magnetic nanoparticles for applications in biomedicine. *Journal of Physics D-Applied Physics, 36*, R198–R206.

Berry, C. C., Wells, S., Charles, S., Atchison, G., & Curtis, A. S. G. (2004). Cell response to dextran derivatised iron oxide nanoparticles post internalization. *Biomaterials, 25*(23), 5405–5413.

Beppu, M. M., & Santana, C. C. (2002a). Influence of calcification solution on in vitro chitosan mineralization. *Materials Research, 5*(1), 47–50.

Beppu, M. M., & Santana, C. C. (2001b). In vitro biomineralization of chitosan. *Key Engineering Materials, 192–195*, 31–34.

Bhattarai, N., Edmondson, D., Veiseh, O., Matsen, A. F., & Zhang, M. (2005). Electrospun chitosan-based nanofibers and their cellular compatibility. *Biomaterials, 26*, 6176–6184.

Brewer, H. S., & Selina, J. (2002). Detection of DNA hybridization on gold surfaces by polarization modulation infrared reflection absorption spectroscopy. *Langmuir, 18*, 4460–4464.

Bulte, J. W., Douglas, T., Witwer, B., Zhang, S. C., Strable, E., Lewis, B. K., et al. (2001). Magnetodendrimers allow endosomal magnetic labeling and in vivo tracking of stem cells. *Nature Biotechnology, 19*(12), 1141–1147.

Cartmell, S. H., Dobson, J., Verschueren, S. B., & EI Haj, A. J. (2002). Development of magnetic particle techniques for long-term culture of bone cells with intermittent mechanical activation. *IEEE Transaction on Nanobioscience, 1*(2), 92–97.

Chang, Y. C., & Chen, D. H. (2005). Adsorption kinetics and thermodymanics of acid dyes on a carboxymethyl chitosan-conjugated magnetic nano-absorbent. *Macromolecular Bioscience, 5*, 254–261.

Cheng, F. Y., Su, C. H., Yang, Y. S., Yeh, C. S., Tsai, C. Y., Wu, C. L., et al. (2005). Characterization of aqueous dispersions of Fe_3O_4 nanoparticles and their biomedical applications. *Biomaterials, 26*, 729–738.

Choi, C. Y., Kim, S. B., Pak, P. K., Yoo, D., II, & Chung, Y. S. (2007). Effect of *N*-acylation on structure and properties of chitosan fibers. *Carbohydrate Polymers, 68*(1), 122–127.

Coche-Guerente, L., & Desbrieres, J. (2005). Physicochemical characterization of the layer-by-layer self-assembly of polyphenol oxidase and chitosan on glassy carbon electrode. *Electrochimca Acta, 50*, 2865–2877.

Daniel, M. C., & Astruc, D. (2004). Gold nanoparticles: assembly, supramolecular chemistry, quantum-size-related properties, and applications toward biology, catalysis, and nanotechnology. *Chemical Review, 104*, 293–346.

Focher, B., Massoli, A., Torri, G., Gervasini, A., & Morazzoni, F. (1986). High molecular weight chitosan 6-0-sulfate. Synthesis, ESR and NMR characterization. *Die Makromolekulare Chemie, 187*, 2609–26020.

Gupta, A. K., Berry, C., Gupta, M., & Curtis, A. (2003). Receptor-mediated targeting of magnetic nanoparticles using insulin as a surface ligand to prevent endocytosis. *IEEE Transaction on Nanobioscience, 2*(4), 256–261.

Heras, A., Rodriguez, N. M., Ramos, V. M., & Aguiio, E. (2001). *N*-Methylene phosphonic chitosan: a novel soluble derivative. *Carbohydrate Polymers, 44*, 1–18.

Holme, K. R., & Perlin, A. S. (1997). Chitosan *N*-sulfate: a water-soluble polyelectrolyte. *Carbohydrate Research, 302*, 7–12.

Jain, T. K., Morales, M. A., Sahoo, S. K., Leslie-Pelecky, D. L., & Labhasetwar, V. (2005). Iron oxide nanoparticles for sustained delivery of anticancer agents. *Molecular Pharmaceutics, 2*(3), 194–205.

Jia, Z., Shen, D., & Xu, W. (2001). Synthesis and antibacterial activities of quaternary ammonium salt of chitosan. *Carbohydrate Research, 333*, 1–6.

Kc, R. B., Aryal, S., Bhattarai, N., & Kim, HY. (2006). Ceramic modification of *N*-acylated chitosan stablised gold nanoparticles. *Scripta Materiala, 54*, 2029–2034.

Kc, R. B., Aryal, S., Bhattarai, S. R., Bhattarai, N., Kim, C. H., & Kim, H. Y. (2006). Stabilization of gold nanoparticles by hydrophobically-modified polycations. *Journal Biomaterials Science, Polymer Edition, 7*(5), 579–589.

Khor, E., & Lim, L. Y. (2003). Implantable applications of chitin and chitosan. *Biomaterials, 24*(13), 2339–2349.

Kim, D. K., Mikhaylova, M., Zhang, Y., & Muhammed, M. (2003). Protective coating of superparamagnetic iron oxide nanoparticles. *Chemistry of Materials, 15*, 1617–1627.

Kokubo, T., Ito, S., Huang, Z. T., Hayashi, T., Sakka, S., Kitsugi, T., et al. (1990). Ca, P-rich layer formed on high-strength bioactive glass-ceramic A-W. *Journal of Biomedical Materials Research, 24*, 331–343.

Lee, H. S., Kim, E. H., Shao, H., & Kwak, B. K. (2005). Synthesis of SPIO-chitosan microspheres for MRI-detectable embolotherapy. *Journal of Magnetism and Magnetic Materials, 293*, 102–105.

Li, P., Nakanishi, K., Kokubo, T., & de Groot, K. (1993). Induction and morphology of hydroxyapatite, precipitated from metaestable simulated body fluids on sol-gel prepared silica. *Biomaterials, 14*(13), 963–968.

Liao, M. H., & Chen, D. H. (2002). Preparation and characterization of a novel magnetic nano-adsorbent. *Journal of Materials Chemistry, 12*, 3654–3659.

Lillo, L. E., & Matsuhiro, B. (1997). Chemical modifications of carboxylated chitosan. *Carbohydrate Polymers, 34*, 397–401.

Marguerite, R., Pham, L. D., Claude, G., & Michel, M. (1992). Substituent distribution on *O*,*N*-carboxymethylchitosans by H and C NMR. *International Journal of Biological Macromolecules, 14*, 122–128.

Muzzarelli, R. A. A. (1988). Carboxymethylated chitins and chitosans. *Carbohydrate Polymers, 8*, 1–21.

Muzzarelli, R. A. A., Tanfani, F., Emanuelli, M., & Mariotti, S. (1982). *N*-(Carboximethylidene) chitosans and *N*-(carboxymethyl) chitosans: novel chelating polyampholytes obtained from chitosan glyoxylate. *Carbohydrate Research, 107*, 199–214.

Neamnark, A., Rujiravanit, R., & Supaphol, P. (2006). Electrospinning of hexanoyl chitosan. *Carbohydrate Polymers, 66*(3), 298–305.

Pankhurst, Q. A., Connolly, J., Jones, S. K., & Dobson, J. (2003). Applications of magnetic nanoparticles in biomedicine. *Journal of Physics D-Applied Physics, 36*, R167–R181.

Peesan, M., Supaphol, P., & Rujiravanit, R. (2005). Preparation and characterization of hexanoyl chitosan/polylactide blend films. *Carbohydrate Polymers, 60*, 343–350.

Ramay, H. R., Li, Z., Shum, E., & Zhang, M. (2005). Chitosan-alginate porous scaffolds reinforced by hydroxyapatite nano and Micro particles: structural, mechanical, and biological properties. *Journal of Biomedicine in Nanotechnology, 1*(2), 151–160.

Rautaray, D., Mandal, S., & Sastry, M. (2005). Synthesis of hydroxyapatite crystals using amino acid-capped gold nnoparticles as a saffold. *Langmuir, 21*, 5185–5191.

Robert, E., & James, J. S. (1977). Selective colorimetric detection of polynucleotides based on the distance-dependent optical properties of gold nanoparticles. *Science, 277*, 1078–1081.

Sato, T., Iijima, T., Sekin, M., & Inagaki, N. (1987). Magnetic properties of ultrafine ferrite particles. *Journal of Magnetism and Magnetic Materials, 65*, 252–256.

Scherer, F., Anton, M., Schillinger, U., Henke, J., Bergemann, C., Kruger, A., et al. (2002). Magnetofection: enhancing and targeting gene delivery by magnetic force in vitro and in vivo. *Gene Therapy, 9*, 102–109.

Shchukin, D. G., Sukhorukov, G. B., & Mohwald, H. (2003). Biomimetic fabrication of noengineered hdroxyapatite/plyelectrolyte cmposite sells. *Chemistry of Materials, 15*, 3947–3950.

Silva, S. S., Ferreira, R. A. S., Fu, L., Carlos, L. D., Mano, J. F., Reis, R. L., et al. (2005). Functional nanostructured chitosan–siloxane hybrids. *Journal of Materials Chemistry, 15*, 3952–3961.

Song, J., Malathong, V., & Bertozzi, C. R. (2005). Mineralization of synthetic polymer saffolds: a bottom-up approach for the development of artificial bone. *Journal of American Chemical Society, 127*, 3366–3372.

Tien, C. L., Lacroix, M., Ispas-Szabo, P., & Mateescu, M. A. (2003). *N*-Acylated chitosan: hydrophobic matrices for controlled drug release. *Journal of Controlled Release, 93*, 1–13.

Woo, K., Hong, J., Choi, S., Lee, H. W., Ahn, J. P., Kim, C. S., et al. (2004). Easy synthesis and magnetic properties of iron oxide nanoparticles. *Chemistry of Materials, 16*, 2814–2818.

Wyrna, D., & Beyer, N. (2002). One-dimensional arrangements of metal nanoclusters. *Nano Letters, 2*, 419–421.

Xie, W., Xu, P., Wang, W., & Liu, Q. (2002). Preparation and antibacterial activity of a water-soluble chitosan derivative. *Carbohydrate Polymers, 50*, 35–40.

Zhang, Y., Kohler, N., & Zhang, M. (2002). Surface modification of superparamagnetic magnetite nanoparticles and their intracellular uptake. *Biomaterials, 23*(7), 1553–15561.

Zhang, C., Ping, Q., Zhang, H., & Shen, J. (2003). Synthesis and characterization of water-soluble *O*-succinyl-chitosan. *Europien Polymer Journal, 39*, 1629–1634.